Nano Energy 40 (2017) 65–72

Contents lists available at ScienceDirect

Nano Energy

journal homepage: www.elsevier.com/locate/nanoen

Full paper

Fingertip-inspired electronic skin based on triboelectric sliding sensing and porous piezoresistive pressure detection

Haotian Chen[a,b], Liming Miao[b], Zongming Su[b], Yu Song[b], Mengdi Han[b], Xuexian Chen[a,b], Xiaoliang Cheng[b], Dongmin Chen[a], Haixia Zhang[a,b,*]

[a] Academy for Advanced Interdisciplinary Studies, Peking University, Beijing 100871, China
[b] National Key Lab of Nano/Micro Fabrication Technology, Institute of Microelectronics, Peking University, Beijing 100871, China

ARTICLE INFO

Keywords:
Fingertip-inspired
Porous carbon nanotube elastomer
Triboelectric generator
Self-powered sliding sensing
Porous piezoresistive detection

ABSTRACT

Fingertip is the region with the largest density of mechanoreceptors in human body. Inspired by its complicated anatomical structure, we design a fingertip-like electronic skin (e-skin) that can simultaneously detect the movements from lateral and vertical directions. The device includes three parts that correspond to fingerprint, epidermis and dermis of the human being, respectively. The fabricated double spiral carbon nanotube-polydimethylsiloxane (CNT-PDMS) electrodes and substrate mimic the structure of fingerprint and epidermis, respectively. Based on triboelectrification effect, the double spiral CNT-PDMS electrodes can generate alternating voltage with different frequencies when sliding across different rough surfaces, which behaves like fast adapting (FA) in real skin. Porous CNT-PDMS is used for detecting pressure, mimicking the function of slow adapting (SA) and the structure of dermis. A cost efficient way to fabricated porous CNT-PDMS is adopted and it can modulate the porosity and resistance at the same time, which provides a way to modulate its sensitivity. With the help of both sliding sensing and pressure sensing, this device can execute many complicated tasks such as differentiating roughness of surfaces and holding-releasing execution, which greatly expands the application fields of e-skin.

1. Introduction

Human skin is a one of the most remarkable organs that covers the entire body and has the ability of sensing multiple external stimuli at the same time. Inspired by the unique structure of human skin, electronic skin (e-skin) integrates various electronic devices together and provides possibilities to mimic the nature of real skin. In recent years, the rapid development of e-skin enables a diverse set of potential applications including wearable devices [1], health monitoring [2–4] and smart robots [5–7].

From a physiological view, human skin mainly includes two layers—epidermis and dermis, and contains four kinds of sensory cells or mechanoreceptors [8]. In general, sensory cells near the skin surface such as Meissner corpuscles and Merkel discs will react only to adjacently applied stimuli, while cells localized more deeply like the Ruffini endings and Pacinian corpuscles will react to stimuli applied farther away. Meissner corpuscles respond to light touch, and adapt rapidly to changes in texture (vibration frequency around 50 Hz). Ruffini endings detect tension deep in the skin and fascia. Merkel discs detect sustained pressure. Pacinian corpuscles in the skin and fascia detect rapid vibrations (of about 200–300 Hz) [9]. According to the speed of adaptation behavior, sensory cells can be classified into slowly adapting (SA) or fast adapting (FA) [10,11]. SA responds to sustained touch and pressure while FA responds to dynamic touch and vibration stimuli. The highest density of mechanoreceptors is found at the fingertips and add up to 250 receptors per square centimeter [12]. What's more, the surface structure of fingerprint can further enhance the sensitivity. As a result, fingers are the most sensitive organs providing us plenty of information. Based on the researches from physiology, scientists and engineers have adopted various methods to mimic these properties of real skin [13–15].

Traditional sensing mechanisms including resistance [16,17] and capacitive sensors [18,19] have the capability of mimicking SA as they can maintain the signal produced by stimuli. Plenty of works have shown their outstanding performances, some of which have already surpassed the property of human beings [4,20]. Among them, piezoresistive sensors are more widely used due to their attractive advantages of simple fabrication process and easy detection method. In order to enhance the stretchability and sensitivity of piezoresistive sensor for epidermal applications, conductive porous structure [21,22] is introduced due to its combination of remarkable electrical conductivity and excellent mechanical properties at the same time.

* Corresponding author at: National Key Lab of Micro/Nano Fabrication Technology, Peking University, Beijing 100871, China.
E-mail address: zhang-alice@pku.edu.cn (H. Zhang).

http://dx.doi.org/10.1016/j.nanoen.2017.08.001
Received 4 June 2017; Received in revised form 18 July 2017; Accepted 1 August 2017
Available online 04 August 2017

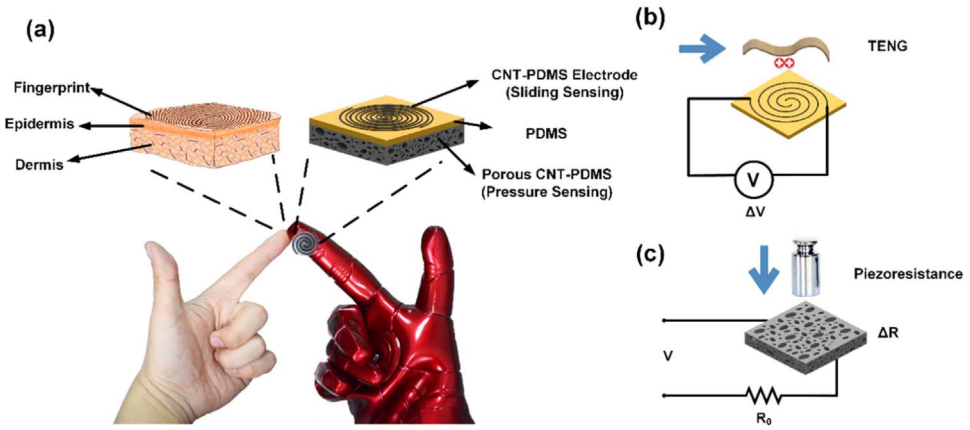

Fig. 1. Schematic diagram of the fingertip-inspired electronic skin. (a) Basic structure of e-skin verses human skin. (b) Sliding sensing part and its working principle. (c) Pressure sensing part and its working principle.

For FA, piezoelectric [23,24] and triboelectric effects [25] are two common-used strategies as they can sense very tiny stimuli and response very fast. Compared to piezoelectric sensor, triboelectric nanogenerator (TENG) is more attractive in e-skin as its low limitation to specific material, which provides much convenience for fabricating stretchable electronic devices, as well as reducing cost at the same time [26–28]. Freestanding TENG [29], one of the four basic working modes of triboelectric generator, possessing both high transfer efficiency and convenient working environment, is widely used as an effective sensing element in various application fields [30,31].

In this work, we propose a fingerprint inspired e-skin with the capability of sensing sliding and pressure at the same time. In order to mimic the physiological structure of fingerprint, epidermis and dermis of human finger, respectively, the sensor composes three layers: a double spiral electrode layer, a pure PDMS layer and a porous CNT-PDMS layers. The fingerprint-like TENG with double spiral-shape CNT-PDMS electrodes is designed for the first time to detect sliding motion, mimicking the function of FA. Based on the frequency of the output voltage rather than the amplitude of TENG, this mechanism creatively provides a digital and visualized method for roughness sensing. Meanwhile, pressure sensing utilizes the piezoresistive of porous CNT-PDMS, which acts like SA in human skin. The sensitivity can be modulated by the resistance and porosity of this porous composite elastomer. A formula is deducted based on porous solid and percolation theory, which provides a guidance for sensitivity modulation. As a proof of concept, the sensor is equipped onto a real finger to detect the roughness of textile. What's more, by integrating the ability of sensing sliding and pressure simultaneously, it can execute complicated tasks such as holding and releasing a bottle repeatedly, suggesting its potential across various applications.

2. Experiment

2.1. Fabrication of CNT-PDMS

CNTs were purchased from Boyu Co., China with length of 10 μm. Firstly, 5 g CNTs were mixed with PDMS base(Dow Corning, Sylgard 184) at the mass fraction needed. 20 ml toluene was added into the mixture of CNTs and PDMS with volume ratio of 4:1. Then the mixture of these three kinds of material was stirred for 6 h using magnetic stirring apparatus. After CNTs were well mixed into PDMS with the help of toluene, the mixture was poured into an evaporating dish to evaporate residual toluene. The cross-linking agent of PDMS can not be added until the toluene was thoroughly removed. At last, the mixture of only PDMS and CNT was baked on the hot plate at temperature of 100 °C for half an hour to solidify them together. More experiment result of CNT-PDMS can be found in Fig. S5.

2.2. Fabrication of spiral shape of CNT-PDMS

A 3D-print mould with groove of double spiral shape was fabricated at first. Then unsolidified CNT-PDMS mentioned above was poured onto the mould and filled the groove. Residual CNT-PDMS outside of the groove can be removed using knife-coating method. Afterwards, the mould together with CNT-PDMS was put onto the hot plate at 70 °C for 4 h. When the double spiral CNT-PDMS was solidified, pure liquid PDMS was poured onto the electrode and baked together. At last, a pure PDMS layer with double spiral CNT-PDMS electrode was peeled off from the mould.

2.3. Fabrication of porous CNT-PDMS

Sugar particles with average size of about 800 μm * 500 μm * 200 μm was purchased from market. By mixing them with unsolidified CNT-PDMS with different weight ratio(1:2, 1:3, 1:4) and baked to solidify CNT-PDMS, a mixture of CNT-PDMS and sugar can be obtained. Then the mixture was then dipped into water to make sugar dissolved. After the sugar particles were removed thoroughly, the porous CNT-PDMS was completely fabricated.

2.4. Characterization

The structure and morphology of the materials are characterized using SEM (Quanta 600 F, FEI Co.). The mechanical measurements of the samples are carried out using a push-pull gauge (Handpi Co.). Additionally, the voltage is amplified by a SR560 low-noise voltage amplifier from Stanford Research Systems and measured via a digital oscilloscope (Agilent DSO-X 2014A)

3. Results and discussion

Fig. 1a shows the basic structure of the device. Inspired by the basic anatomical structure of fingertip, the device is divided into three parts: double spiral CNT-PDMS electrode layer, pure PDMS layer and porous CNT-PDMS layer, each of which mimicking fingerprint, epidermis and dermis, respectively. Double spiral CNT-PDMS electrodes layer are used for sliding detection, working as a freestanding TENG as shown in Fig. 1b. When an object contacts to the device, there would be a charge separation due to the property of different materials according to the triboelectric sequence [32]. During the movement of object across the surface of the device, an alternating voltage will be generated due to electrons transferring between two electrodes. In this way, sliding motion is detected and the roughness of the object can be reflected according to the number of peaks of the voltage. On this basis, rougher object tends to generate more peaks during the sliding motion, providing a new visual solution for the qualitatively detection of surface roughness. Porous CNT-PDMS layer is used for pressure detection based

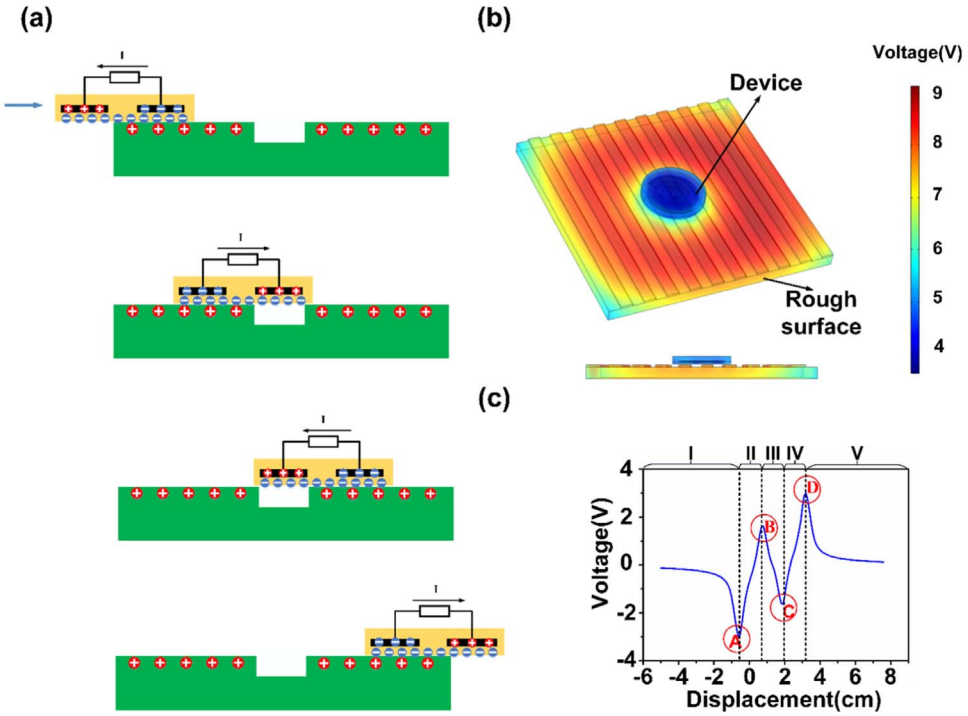

Fig. 2. Basic working principle of the TENG part. (a) Working process with how the charges transferring between electrodes. (b) Three-dimension FEA model showing how potential distributes. (c) Simulated result reflecting the working process in detail.

on change of contact resistance under compression as shown in Fig. 1c, which can enhance the sensitivity dramatically. By changing the content of CNTs and mix ratio of CNT-PDMS and sugar in the fabrication process of this porous composite elastomer, the resistance and porosity can be well regulated. The detailed fabrication process can be found in Fig. S1 in Supporting information.

Working principle of the TENG is demonstrated in Fig. 2a. One-gap target object and double spiral electrodes device are taken as example to explain and analyze the waveform for convenience. As the device is fabricated with PDMS, which is a typical material prone to attract electrons, the device would carry more negative charges while the surface of the target object would carry more positive charges with the same amount after their contact to each other. Four key positions, where the current direction would reverse, are chosen to describe the whole process. Three-dimensional finite element analysis (FEA) of the process is shown in Fig. 2b in which the left electrode is defined as positive electrode while right electrode is defined as negative one. Corresponding simulated result is demonstrated in Fig. 2c, in which four key positions mentioned above are marked as A, B, C and D. Position A corresponds to the condition that right electrode is fully above the object while the left one has not reached the object surface yet. Position B means the location where right electrode suspends above the air gap and left electrode still contacts the object. As the device continues to move, left electrode gets to the air gap while the right one comes back to the object surface and this condition is marked as Position C. Similar to Position A, Position D corresponds to the location that right electrode just moves out of the object while left electrode still stays on the object. More simulation results of potential difference between the two electrodes during the movement is shown in Fig. S4.

The whole process can be further divided into five sub-processes, defined by the four key positions mentioned above. Each sub-process is carefully studied to describe the whole process in detail. Processes I-V correspond to: before Position A, between Position A and Position B, between Position B and Position C, between Position C and Position D and after Position-D, respectively. Each time the device reaches the key position, the output voltage reaches a maximum or minimum value. In each process, the direction of the current is unchanged. The directions of current are inverse in neighboring processes.

In Process I, as the e-skin moves close to the target object, more negative charges will be induced in right electrode, thus producing a current flowing from right to left shown in Fig. 2c. When the device moves to the Position A, the voltage will reach the valley for the first time.

In Process II, at first, left electrode begins to move onto the target object surface and more negative charges are induced in the this electrode to reach electrostatic equilibrium, generating a current from left to right. Then right electrode begins to move to the air gap. More positive charges will be induced in the right electrode because of separation from the surface, therefore, electrons continue to move from left to right and the current direction is unchanged. As the device gets to Position B, the voltage gets to the peak value for the first time.

For Process III, right electrode moves far away from the air gap while left electrode moves close to it. More positive charges are induced in the left electrode and more negative charges are induced in the right one, producing a current flowing from right to left and the current direction is changed as shown in Fig. 2c. The voltage reaches the valley for the second time when the device gets to Position C.

In Process IV, as left electrode moves away from the air gap, positive charges will flow from left electrode to right electrode, so the current direction reverses again. Then the right electrode begins to move out of the object surface, more positive charges will be induced in right electrode, so the current still flows from left to right. When the device moves to Position D, output voltage gets to the peak value for the second time.

In Process V, right electrode is already out of the surface while left electrode is moving out. Symmetrical to Process I, positive charges move from right electrode to left and the electric current direction changes for the fifth time.

The number of air gaps, the size of electrode and the number of electrode pair will all affect the waveform. In order to analyze how the number of air gaps, *n*, influence the output, three kinds of device with no-gap, one-gap and two-gap, are designed. Simulated results is shown in Fig. 3a. As discussed before, more air gaps can result in more peaks and valleys, giving a visualized method for roughness detection. It is worthy noting that even no-gap can also generate voltage when the device comes close the object and moves out of the object, which

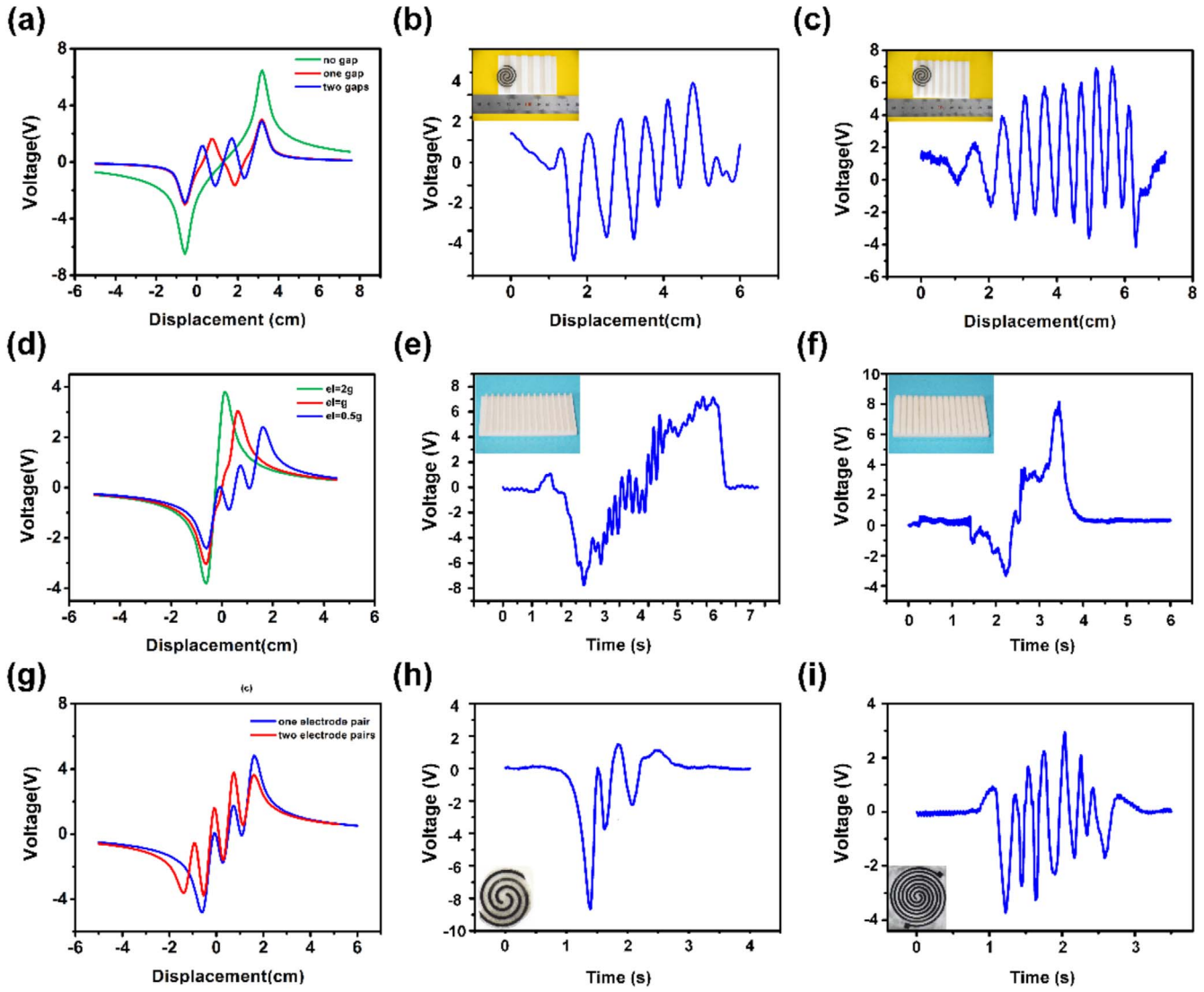

Fig. 3. Key parameters influencing the result and real measurement results. (a) Simulated result showing how the number of gap influence the output. (b) Measurement result with a 4-gap model. (c) Measurement result with a 7-gap model. (d) Simulated result showing how the length of electrode and gap influence the output. (e) Measurement result of model with 12 wider gaps ($g = 2el$). (f) Measurement result of model with 12 narrower gaps ($el = 2g$). (g) Simulated result showing how the number of electrode pair influence the output. (h) Measurement result of the device with 1.5 cycles of spiral. (i) Measurement result of the device with 4.5 cycles of spiral.

demonstrates that sliding movement on flat surface can also be detected. In order to verify the conclusion drawn from simulation, two target objects with 4 air gaps and 7 air gaps, respectively, are fabricated using 3D printer. Both of them have the same length of 6 cm and width of 4 cm, respectively. A sample device with 3 cycles of spiral and 1 mm-wide electrode is fabricated to move across these models, ensuring that the device can work smoothly. The numbers of wave are consistent with the simulation results as shown in Fig. 3b and Fig. 3c.

The size of electrode, is a very significant parameter for detecting roughness. The width of electrode is defined as *el* and the air gap on the target object is defined as *g*. Three combinations, $el = 0.5g$, $el = g$ *and* $el = 2g$, are considered and the simulated results are demonstrated in Fig. 3d. Device with one cycle of double spiral electrodes and two air gaps is taken to simulate for convenience. In the situation of $el = 2g$, the waveform in green is almost like the situation that target object has no air gap on its surface, meaning that the device can't detect the roughness while $el > g$. As $el = g$, which is a crucial point, the device just can monitor the topography of the surface with very slight fluctuation as shown in Fig. 3d in red line. When $el = 0.5g$, the waveform in blue can explicitly reflect the location of air gap. From comparison three sets of *el* and *g*, the detection limitation is dependent on the relative size of them two. Only when the length of gap is larger than the width of electrode, the device can operate properly. Two special designed models, each of which has 12 gaps on the surface, were fabricated by 3D printer. One model has wider gap ($el = 0.5g$) and the other has narrower gap ($el = 2g$). The experiment result of the first model is shown in Fig. 3e. It can be seen from the result that the sensor can work effectively. However, for the model with narrower gap, the TENG signal is not obvious as the former one as shown in Fig. 3f.

The number of electrode pairs, *m*, can also influence the number of the wave. The result shown in Fig. 3g indicates that one more cycle will increase one more valley and peak, which is easy to deduce from the working principle. Two samples with different numbers of cycle of spiral electrode were fabricated to support the simulated result. One sample has 1.5 cycles of spiral while the other has 4.5 cycles of spiral. Both of them have the same width of electrode and were used to slide across the same 3D printed model. From the measurement results shown in Fig. 3h and Fig. 3i, increased number of cycles of spiral electrode will increase the number of voltage waves. Multiplication of the number of cycles of spiral electrode can enlarge effective area for detection.

What's more, single electrode TENG can also be used for such

function with spiral shape working as a single-electrode TENG [33]. However, the simulated result of Fig. S7 demonstrates that single-electrode TENG is not an optimal choice due to its weak resolution in spite of its simple fabrication process and easy integration. Though the wave generated from single-electrode TENG is more symmetric and can identify the location of air gap exactly, the little peak is almost invisible and easy to be covered by noise in actual test. In this way, single-electrode scheme is replaced by double-electrode mode, which is used in real devices. Three or more electrodes can also used for roughness detection with the same mechanism, however, more electrodes will enhance fabrication complexity and increase more channels when tested. So TENG with double spiral CNT-PDMS electrodes is adopted in the device.

Porous CNT-PDMS is fabricated for pressure sensing due to its unique characteristic of combining both conductive elastomer and porous material, which is beneficial for enhancing the sensitivity. The electrical resistance can be adjusted by the content of CNTs and the porosity can be modulated via mixing CNT-PDMS with sugar particles in different mass fraction. Three kinds of resistivity of porous CNT-PDMS are prepared by mixing 4 wt%, 5 wt% and 6 wt% CNT into PDMS and marked as *C4*, *C5* and *C6*, respectively. Meanwhile three kinds of porosity of porous CNT-PDMS are also fabricated by mixing with sugar at the mass fraction of 1:2, 1:3 and 1:4, marked as *M2*, *M3* and *M4*, respectively. Considering all the compound modes mentioned above, there are 9 samples with different CNT contents and porosities and marked as *CmMn* ($m = 4, 5, 6$ and $n = 2, 3, 4$).

SEM images of *C6M2*, *C6M3* and *C6M4* are displayed in Fig. 4a-c to observe their porous properties. It's obvious that only surface part has the porous structure for *C6M2* and inner space is almost like a rigid materials from Fig. 4a. Because the amount of sugar particles is so little that the particles are almost separate from each other, after the mixture of CNT-PDMS and sugar particles was dipped into water, only particles on the surface dissolved. For *C6M3*, compared with former sample, number of pores increases and porous structure appears in deeper part. However, the volume of porous structure is still limited as shown in Fig. 4b. Final SEM image shows the morphology of *C6M4*. The number

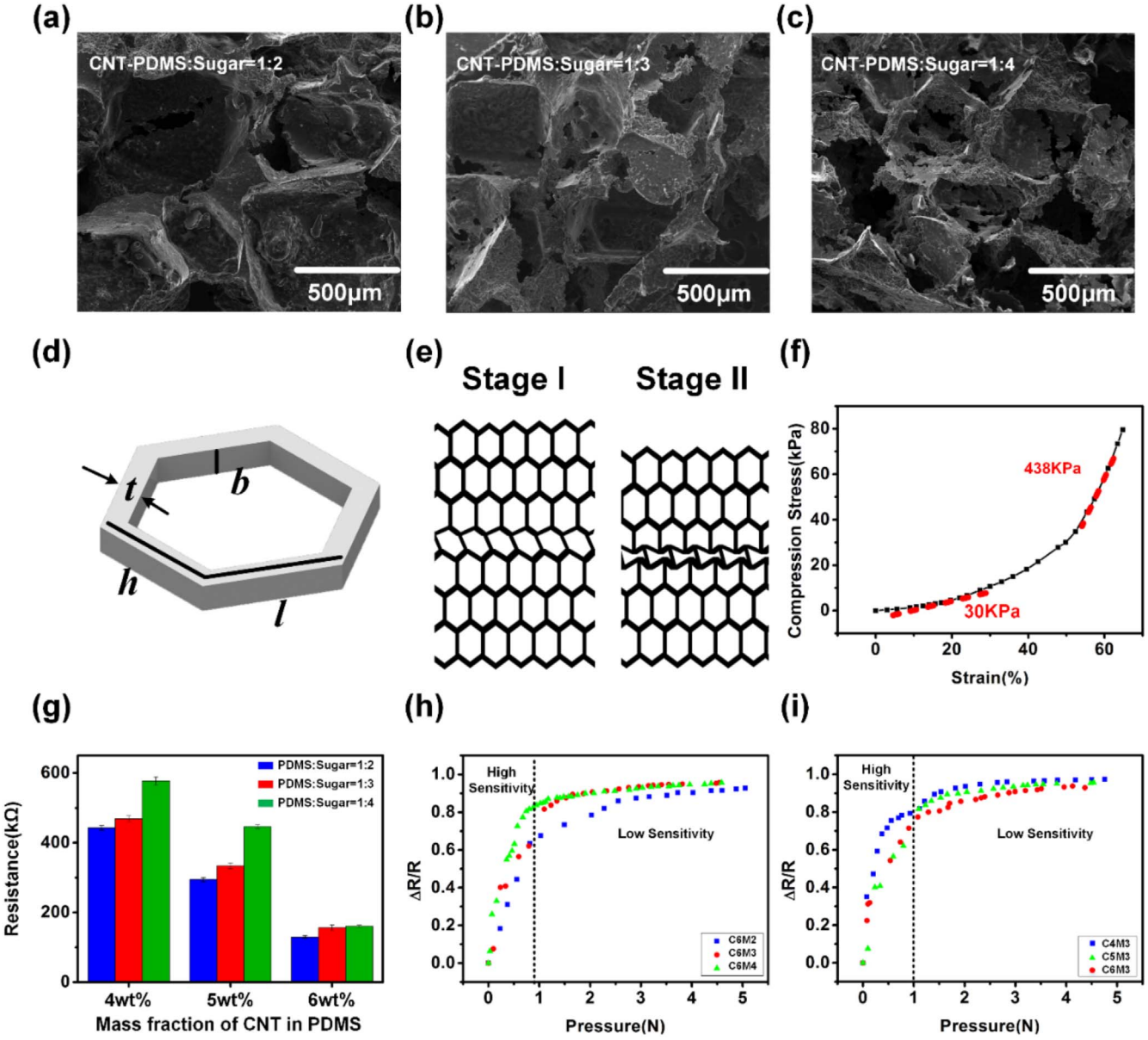

Fig. 4. Basic characteristics of porous CNT-PDMS used for pressure detection. (a)-(c) SEM images of C6M2, C6M3 and C6M4. (d) Stain-stress curve of porous CNT-PDMS. (e) Ideal honeycomb model for calculation. (f) Demonstration for two compression processes. (g) Origin resistance for different samples. (h) Piezoresistive responsive curve for the same CNT contents while different amount of pores. (i) Piezoresistive responsive curve for the same amount of pores while different CNT contents.

of pores is much larger than former two and in deeper district there are only black holes without rigid part, which is clear to see in Fig. 4c. More SEM images of CNTs is shown in Fig. S2 in Supporting information.

To analyze the mechanism of the piezoresistive effect of the device, a classic honeycomb model is adopted shown in Fig. 4d [34]. h and l are two kinds of length of the honeycomb, t is the thickness of the wall and b is the depth. The whole compression process of porous can be briefly divided into two stages as shown in Fig. 4e. In the first stage, the wall of the porous structure bends and collapses. When it comes to the second stage at higher strain, the cells collapse sufficiently and further deformation compresses the cell wall material itself. In this stage, most of air has been squeezed out and most the cell walls have been stacked together. So the Young's modulus is almost the same as that of rigid material.

With the help of ideal honeycomb model, Young's modulus corresponding to these two stages can be calculated:

$$E_1 = \frac{n^2\pi^2}{24}\cdot\frac{t^3}{lh^2}\cdot\frac{1}{\cos(\theta)}E_s \tag{1}$$

$$E_2 \approx E_s \tag{2}$$

where, E_s is the Young's modulus of the material, θ is the angle between h and l and I is the second moment of inertia of the cell wall ($I = bt^3/12$ for a wall of uniform thickness t). In the ideal model, where $h=l$, $E_1 = 0.22(t/l)^3E_s$. Detailed calculation process can be found in S3 in Supporting information.

Stain-stress curve is shown in Fig. 4f, which clearly demonstrates the two compression stages. In Stage I, the Young's modulus of 30 kPa can be calculated from the measurement result, which is rather small compared with rigid PDMS. Assuming honeycomb is regular hexagon, E_1 is about one-tenth of E_s. In Stage II, the Young's modulus increases to 438 kPa, which is in the range of Young's modulus of pure PDMS, indicating that most of air has been squeezed out of the porous structure.

Fig. 4g shows the origin resistances of the 9 samples. Two main trends can be found from the test results. The first is the more CNT contents, the lower the resistance the sample gains, which is proved and tested by plenty of works [35–37]. The second is as the number of pores increases, the resistance also rises up. According to the formula of resistance:

$$R = \frac{l}{\sigma\cdot A} \tag{3}$$

where R is the resistance, l is the length, A is the cross area and σ is conductivity. Porous structure make cross sectional area decreased and the length increased so the total resistance will increase. What's more, the second trend is more obvious in high resistance samples. Porous CNT-PDMS with lower content of CNT can be regarded as the sample with lower conductivity. Smaller σ make resistance increase much more than larger σ.

Changed resistance compared with the original resistance is often used for measure the sensitivity and can be written as

$$\Delta R = \frac{\Delta l}{\sigma\cdot A} - \frac{l\Delta A}{\sigma\cdot A^2} - \frac{l\Delta\sigma}{\sigma^2\cdot A} \tag{4}$$

$$\frac{\Delta R}{R} = \frac{\Delta l}{l} - \frac{\Delta A}{A} - \frac{\Delta\sigma}{\sigma} \tag{5}$$

Sensitivity (S) is defined as $S = \Delta(\Delta R/R)/\Delta\varepsilon$, where ε is the pressure exerted on the sensor. So the sensitivity can be written as

$$\frac{\Delta R/R}{\Delta\varepsilon} = \frac{\Delta l/l}{\Delta\varepsilon} - \frac{\Delta A/A}{\Delta\varepsilon} - \frac{\Delta\sigma/\sigma}{\Delta\varepsilon} \tag{6}$$

According to the definition of Young's modulus, where $E = \frac{\Delta\varepsilon}{\Delta l}$, the first term of Eq. (6) can be expressed as $\frac{1}{E\cdot l}$. From the conclusion in the percolation theory [38], the last term is dependent on the content of CNTs with the relationship of:

$$\frac{\Delta\sigma/\sigma}{\Delta\varepsilon} \propto (P - P_c)^{\alpha} \tag{7}$$

where P is the content of CNTs, P_c is the percolation threshold of CNT content which can just form the conductive network and α is the factor associated with the geometrical feature. As the cross area of the porous CNT-PDMS is almost unchanged, so $\Delta A \approx 0$. In this way, the sensitivity can be rewritten as:

$$\frac{\Delta R/R}{\Delta\varepsilon} = \frac{1}{E\cdot l} - k\cdot(P - P_c)^{\alpha} \tag{8}$$

where k is the coefficient to reflect the relationship between the conductivity and the CNT content.

From the analysis above, the sensitivity of the device is mainly attributed to the porosity, which will influence the effective Young's modulus (E), and content of CNTs (P) which will influence the property of the conductive network. The porosity can be modulated by the mass fraction of sugar particle mixed with the CNT-PDMS and the conductivity can be directly adjusted by amount of CNT mixed with pure

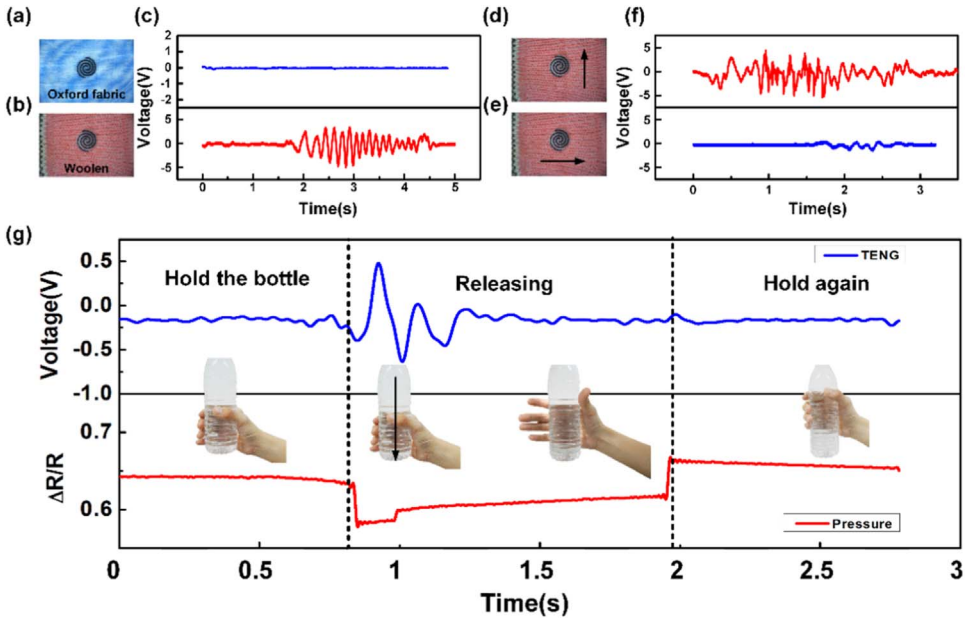

Fig. 5. Applications demonstration of this multifunctional sensor. (a) and (b) demonstrate that the sensor move across different kinds of textiles, Oxford fabric and woolen, with different roughnesses. (c) Output voltages from TENG for different textiles. (d) and (e) demonstrate that the sensor move in different directions. (f) Output voltage from TENG due to different directions. (g) Signals of both TENG voltage and changed resistance to estimate whether the bottle is held firmly or not.

PDMS. In this way, the final sensitivity can be well modulated.

Fig. 4h demonstrates piezoresistive responsive curve for the same CNT contents while different amount of pores. Two sensitivity ranges can be seen from the test results, corresponding to the two compression stages. In the first compression stage, the effective Young's modulus is rather small. From the Eq. (8), lower Young's modulus results in higher sensitivity. As the porous CNT-PDMS continues to be compressed, the Young's modulus increase to its original range, which cause the sensitivity to decrease. What's more, the more sugar particles mixed with CNT-PDMS, the more pores will be produced, which can enhance the porosity and lower Young's modulus of the whole material. In this way, the sample C6M4 has the highest sensitivity when the CNT contents are the same.

Piezoresistive responsive curve for the same amount of pores while different CNT contents is shown in Fig. 4i. Similar trend with two sensitivity ranges can be observed which can also be explained due to the two compression stages. Besides the influence resulted from the porosity, the content of CNT also has impact to the final result. When the content of CNTs is larger than the percolation threshold, increased CNTs will enhance the conductivity while lower its sensitivity to external pressure. In this way, lower CNT content results in higher sensitivity of the sensor, which is clear to see in the picture.

This fingertip-inspired sensor can be used in many fields. Fig. 5 shows its potential for different application areas. Fig. 5a and Fig. 5b show that the e-skin moves across two kinds of textiles, Oxford fabric and woolen, with different roughnesses. During this process, the spiral-shape TENG can generate voltage with different frequencies, which are useful for robot to identify the object it touches. Oxford fabric is a smoother textile, which can hardly generate effective output voltage. Compared to Oxford fabric, woolen is much rougher. When sliding across woolen, the TENG can output alternating voltage, showing its ability for distinguishing roughness. The test results are shown in Fig. 5c. Due to the spiral shape of electrode, the sensor can also detect anisotropy of roughness. As shown in Fig. 5d and Fig. 5e, the pattern of woolen is like a grating groove. When the sensor slides perpendicular to the direction of groove, the TENG can work effectively producing higher-frequency voltage as it move across more grates. However, as the sensor move along the groove, the TENG only generate lower-frequency voltage with lower voltage as shown in Fig. 5f. With this property, the sensor can distinguish the pattern of the surface.

What's more, by combining both sliding sensing and pressure sensing, a robot can execute more complex task with this sensor system. A demonstration of holding a bottle of water, releasing and holding it again is shown in Fig. 5g. At first, the bottle is firmly hold by hand. The sliding element remains no signal while the pressure element maintains a higher level, indicating the bottle is griped firmly by hand with great strength. As the pressure is decreasing gradually, static friction will turn to sliding friction. In this process, the TENG is activated due to the sliding of the bottle and gives rise to a alternating voltage as shown in the picture. As the pressure continues to decrease, hand is fully separated from the bottle and signal of TENG weakens. At that time, the robot can realize that it failed to hold the bottle so it increase the pressure again until the bottle is griped again. When the bottle is held again, the sliding element stops to work and the pressure recover to original level. The whole process can be seen in video (Supporting Video 1) in which the pressure changed gradually. In order to demonstrate the sensing system can detect different pressures in such complex situation, similar process in which the pressure changed violently is demonstrated in video (Supporting Video 2). The whole process is very like the way of skin receptors working for human beings. Two kinds of skin receptors, SA and FA, work in different ways. For SA, it always awakes with lower sensing frequency, which is like the pressure sensing element. FA only works when a sudden signal occurs and responds to higher frequency, which works like the sliding sensing element.

4. Conclusion

In summary, this paper demonstrates a fingertip-inspired e-skin that mimics the three fundamental parts (i.e., fingerprint, epidermis and dermis) in anatomical structure of fingertip by splitting a stretchable sensor into three different parts. Such an e-skin includes a freestanding TENG that use double spiral CNT-PDMS electrodes to detect sliding motion, mimicking fingerprint. The TENG generates voltage with different frequencies to reflect the roughness of the surface due to the transferred of charges between two electrodes during sliding across the surface. The precision can be improved by designing the size of electrode. The piezoresistive sensor integrated in the e-skin utilize porous CNT-PDMS as the piezoresistive material to mimic the function of dermis. Both of the resistance and porosity can influence the final sensitivity. Two regions with different sensitivities during the compression process are observed due the property of porous structure. By controlling the mass fraction of CNT and weight ratio of sugar particles, the sensitivity can be well modulated, which is very useful for different application areas. A pure PDMS layer is stacked between two functional layers to avoid their interference, acting as the structure of epidermis in human. Finally, because of the ability of sensing pressure and sliding simultaneously, robot with this sensor can manipulate more complex tasks such as roughness detection and holding/releasing a soft bottle. Such a bio-inspired structure of electronic skin provides new routes of combining different sensing mechanisms. Taking advantage of the unique properties of triboelectric and piezoresistive sensing enables more functions and suggests potential in application in various fields.

Acknowledgements

This work was supported by National Key Research and Development Program of China (2016YFA0202701), the National Natural Science Foundation of China (Grant No. 61674004 and 91323304), the Beijing Natural Science Foundation of China (Grant No. 4141002), and the Beijing Science & Technology Project (Grant No. D151100003315003).

Appendix A. Supplementary material

Supplementary data associated with this article can be found in the online version at http://dx.doi.org/10.1016/j.nanoen.2017.08.001.

References

[1] D.-H. Kim, N. Lu, R. Ma, Y.-S. Kim, R.-H. Kim, S. Wang, J. Wu, S.M. Won, H. Tao, A. Islam, Science 333 (2011) 838–843.
[2] J. Park, Y. Lee, J. Hong, M. Ha, Y.D. Jung, H. Lim, S.Y. Kim, H. Ko, ACS Nano 8 (2014) 4689–4697.
[3] X. Huang, Y. Liu, H. Cheng, W.J. Shin, J.A. Fan, Z. Liu, C.J. Lu, G.W. Kong, K. Chen, D. Patnaik, Adv. Funct. Mater. 24 (2014) 3846–3854.
[4] D. Kang, P.V. Pikhitsa, Y.W. Choi, C. Lee, S.S. Shin, L. Piao, B. Park, K.-Y. Suh, T.-i. Kim, M. Choi, Nature 516 (2014) 222–226.
[5] M.L. Hammock, A. Chortos, B.C. Tee, J.B. Tok, Z. Bao, Adv. Mater. 25 (2013) 5997–6038.
[6] S. Bauer, S. Bauer-Gogonea, I. Graz, M. Kaltenbrunner, C. Keplinger, R. Schwodiauer, Adv. Mater. 26 (2014) 149–162.
[7] R.S. Dahiya, P. Mittendorfer, M. Valle, G. Cheng, V.J. Lumelsky, IEEE Sens. J. 13 (2013) 4121–4138.
[8] A.D. Craig, Nat. Rev. Neurosci. 3 (2002) 655–666.
[9] E.D. Adrian, K. Umrath, J. Physiol. 68 (1929) 139–154.
[10] R.S. Johansson, J.R. Flanagan, Nat. Rev. Neurosci. 10 (2009) 345–359.
[11] V.E. Abraira, D.D. Ginty, Neuron 79 (2013) 618–639.
[12] A.B. Vallbo, R.S. Johansson, Hum. Neurobiol. 3 (1984) 3–14.
[13] M. Ha, S. Lim, J. Park, D.-S. Um, Y. Lee, H. Ko, Adv. Funct. Mater. 25 (2015) 2841–2849.
[14] B.C. Tee, A. Chortos, A. Berndt, A.K. Nguyen, A. Tom, A. McGuire, Z.C. Lin, K. Tien, W.G. Bae, H. Wang, P. Mei, H.H. Chou, B. Cui, K. Deisseroth, T.N. Ng, Z. Bao, Science 350 (2015) 313–316.
[15] J. Park, M. Kim, Y. Lee, H.S. Lee, H. Ko, Sci. Adv. 1 (2015).
[16] T. Yamada, Y. Hayamizu, Y. Yamamoto, Y. Yomogida, A. Izadi-Najafabadi, D.N. Futaba, K. Hata, Nat. Nanotechnol. 6 (2011) 296–301.
[17] T. Theodosiou, D. Saravanos, Compos. Sci. Technol. 70 (2010) 1312–1320.

[18] S.C. Mannsfeld, B.C. Tee, R.M. Stoltenberg, C.V.H. Chen, S. Barman, B.V. Muir, A.N. Sokolov, C. Reese, Z. Bao, Nat. Mater. 9 (2010) 859–864.
[19] D.J. Lipomi, M. Vosgueritchian, B.C. Tee, S.L. Hellstrom, J.A. Lee, C.H. Fox, Z. Bao, Nat. Nanotechnol. 6 (2011) 788–792.
[20] Y. Wang, C. Zhu, R. Pfattner, H. Yan, L. Jin, S. Chen, F. Molina-Lopez, F. Lissel, J. Liu, N.I. Rabiah, Z. Chen, J.W. Chung, C. Linder, M.F. Toney, B. Murmann, Z. Bao, Sci. Adv. 3 (2017) e1602076.
[21] H. Chen, Z. Su, Y. Song, X. Cheng, X. Chen, B. Meng, Z. Song, D. Chen, H. Zhang, Adv. Funct. Mater. 27 (2017) 1604434.
[22] J.-W. Han, B. Kim, J. Li, M. Meyyappan, Appl. Phys. Lett. 102 (2013) 051903.
[23] Z.L. Wang, Adv. Mater. 24 (2012) 4632–4646.
[24] W.Z. Wu, Z.L. Wang, Nat. Rev. Mater. 1 (2016).
[25] F.R. Fan, W. Tang, Z.L. Wang, Adv. Mater. 28 (2016) 4283–4305.
[26] S.H. Wang, L. Lin, Z.L. Wang, Nano Energy 11 (2015) 436–462.
[27] H. Guo, Q. Leng, X. He, M. Wang, J. Chen, C. Hu, Y. Xi, Adv. Energy Mater. 5 (2015) 1400790.
[28] J. Chen, H. Guo, X. He, G. Liu, Y. Xi, H. Shi, C. Hu, ACS Appl. Mater. Interfaces 8 (2016) 736–744.
[29] S.H. Wang, Y.N. Xie, S.M. Niu, L. Lin, Z.L. Wang, Adv. Mater. 26 (2014) 2818–2824.
[30] S.H. Wang, S.M. Niu, J. Yang, L. Lin, Z.L. Wang, ACS Nano 8 (2014) 12004–12013.
[31] L. Lin, S.H. Wang, Y.N. Xie, Q.S. Jing, S.M. Niu, Y.F. Hu, Z.L. Wang, Nano Lett. 13 (2013) 2916–2923.
[32] Z.L. Wang, ACS Nano 7 (2013) 9533–9557.
[33] B. Meng, W. Tang, Z. Too, X. Zhang, M. Han, W. Liu, H. Zhang, Energy Environ. Sci. 6 (2013) 3235–3240.
[34] L.J. Gibson, M.F. Ashby, Cellular Solids: Structure and Properties, Cambridge University Press, 1999.
[35] Y. Zhang, C.J. Sheehan, J. Zhai, G. Zou, H. Luo, J. Xiong, Y. Zhu, Q. Jia, Adv. Mater. 22 (2010) 3027–3031.
[36] A. Sepúlveda, R.G. de Villoria, J. Viana, A. Pontes, B. Wardle, L.A. Rocha, Nanoscale 5 (2013) 4847–4854.
[37] L. Ci, J. Suhr, V. Pushparaj, X. Zhang, P. Ajayan, Nano Lett. 8 (2008) 2762–2766.
[38] D. Stauffer, A. Aharony, Introduction to Percolation Theory, CRC Press, 1994.